Reconstruction of the Human Cerebral Cortex from Magnetic Resonance Images

Chenyang Xu, Dzung L. Pham, Maryam E. Rettmann, Daphne N. Yu, and Jerry L. Prince*

Abstract—**Reconstructing the geometry of the human cerebral cortex from MR images is an important step in both brain mapping and surgical path planning applications. Difficulties with imaging noise, partial volume averaging, image intensity inhomogeneities, convoluted cortical structures, and the requirement to preserve anatomical topology make the development of accurate automated algorithms particularly challenging. In this paper we address each of these problems and describe a systematic method for obtaining a surface representation of the geometric central layer of the human cerebral cortex. Using fuzzy segmentation, an isosurface algorithm, and a deformable surface model, the method reconstructs the entire cortex with the correct topology, including deep convoluted sulci and gyri. The method is largely automated and its results are robust to imaging noise, partial volume averaging, and image intensity inhomogeneities. The performance of this method is demonstrated, both qualitatively and quantitatively, and the results of its application to six subjects and one simulated MR brain volume are presented.**

Index Terms—**Cortical surface reconstruction, deformable surface models, fuzzy segmentation, isosurface, magnetic resonance imaging.**

I. INTRODUCTION

RECENT advances in medical imaging of the brain allow detailed anatomical information to be derived from high-resolution imaging modalities such as magnetic resonance imaging (MRI) and computed tomography (CT). These advances have placed a priority on obtaining accurate surface reconstructions of the human cerebral cortex, not only to provide valuable information on the geometric and anatomical properties of the brain, but for other purposes as well. For example, the location of functional activity obtained from

positron emission tomography (PET), functional magnetic resonance imaging (fMRI), and other methods can be mapped to the extracted cortical surface, providing a better understanding of brain function and organization [1]. The reconstructed surfaces can also be warped to other cortical surfaces for the purpose of image registration [2]–[5], digital atlas labeling [6], and population-based probabilistic atlas generation [7].

Geometrically, the human cerebral cortex is a thin folded sheet of gray matter (GM) that lies inside the cerebrospinal fluid (CSF) and outside the white matter (WM) of the brain. Reconstruction of the cortex from MR images is problematic, however, due to difficulties such as imaging noise, partial volume averaging, image intensity inhomogeneities, convoluted cortical structures, and the requirement to preserve anatomical topology. Preservation of topology is important because a reconstructed cortical surface without a correct topology, such as results obtained from isosurface algorithms [8], may lead to incorrect interpretations of local structural relationships and prevents cortical unfolding. These two aspects are critical in applications such as brain morphometric analysis, surgical path planning, and functional mapping.

Recently, there has been a considerable amount of work in this area of research. Mangin *et al.* [9] and Teo *et al.* [10] reconstructed the cortex using a voxel-based method. Volumetric registration, proposed by Collins *et al.* [11] and Christensen *et al.* [12], allows the generation of cortical surfaces from MR brain image volumes, given a template volume and its associated reconstructed cortical surface. Methods of tracing two-dimensional (2-D) contours, either manually or automatically through 2-D image slices followed by contour tiling to reconstruct the cortical surface, have been described by Drury *et al.* [13] and Klein *et al.* [14]. Dale and Sereno [1], MacDonald *et al.* [15], Davatzikos and Bryan [16], and Sandor and Leahy [17] have used methods based on deformable surface models to reconstruct cortical surfaces. Unlike voxel-based methods, a deformable surface is able to deform through a continuum and yield a smooth surface representation of the cortex. A surface representation is critical in applications such as cortical matching and statistical analysis of cortical surfaces (cf., [3]–[5] and [7]). Traditional deformable surface models, however, have difficulties in progressing into convoluted regions, resulting in reconstructed surfaces that lack the deep cortical folds [9], [16], [18].

The goal of the present work is to provide a systematic method for reconstructing a surface representation of the central cortical layer from MR images of the brain. We define the central cortical layer as the layer lying in the

geometric center of the cortex, which is approximately cytoarchitechtonic layer four. Although the proposed method can be tailored easily to track either the GM/CSF interface or the GM/WM interface, we favor using the central cortical layer to represent the cortex because it best represents the overall cortical geometry compared to either the GM/CSF interface or the GM/WM interface [19], [13]. Our method is based on a new deformable surface model consisting of novel approaches for both initializing the deformable surface and deriving the external forces. This deformable surface model is particularly suited to reconstruct the entire central cortical surface including the deep folds, while maintaining the correct cortical topology. The deformable surface model is applied on membership functions computed by an adaptive fuzzy segmentation rather than on image intensity volumes. The segmentation provides modeling of partial volume effects and eliminates dependency on image intensity, which can vary between subjects.

This paper is organized as follows. In Section II, we describe our new cortical surface reconstruction method. In Section III, we present and discuss both qualitative and quantitative results of applying our method to six different subjects, as well as a simulated MR brain volume. Finally, in Section IV, we conclude our paper and point out future research directions.

We note that part of the work reported in this paper has appeared in the conference papers [20] and [21].

II. METHODS

In this section we present our method for reconstruction of the cortical surface from MR brain image data. This method consists of four major steps. First, the acquired data is preprocessed to extract the cerebrum and interpolated to cubic voxels. Second, the brain image volume is segmented into fuzzy membership functions of GM, WM, and CSF tissue classes using an adaptive segmentation algorithm that is robust to image intensity inhomogeneities. Third, an iterative process of median filtering and isosurface generation on the WM membership function produces an initial estimate of the cortical surface that is topologically correct. Fourth, our deformable surface algorithm moves this surface toward the central layer of the cortex, yielding the final reconstructed cortical surface. Fig. 1 shows an overall flow diagram of our method. Throughout this section, we use results from one subject as an example to illustrate the method.

A. Data Acquisition and Preprocessing

Our algorithm uses T1-weighted volumetric MR image data acquired on a GE Signa 1.5 Tesla MR scanner using the SPGR imaging protocol (TR = 35 ms, TE = 5 ms, flip angle =45°, NEX = 1). This data provides adequate contrast between gray matter, white matter, and cerebrospinal fluid and has fine enough resolution to resolve the complex structure of the cortex. It has been tested on both axially acquired image data with in-plane resolution of 0.9375 × 0.9375 mm and out-of-plane resolution of 1.5 mm and on coronal data with comparable resolution figures. The algorithm is easily modified
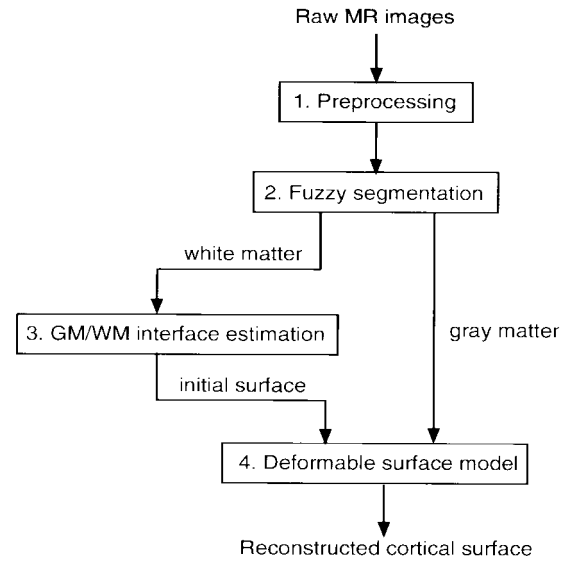

Fig. 1. Block diagram of the overall cortical surface reconstruction system.

to use multispectral data, but the resolution must be the same or better.

The first step in our method is to preprocess the image volume to remove skin, bone, fat, and other noncerebral tissue. We used a semiautomated software package developed by Christos Davatzikos at the Johns Hopkins University [22]. This package features a combination of region-growing algorithms and mathematical morphology operators to ease the processing of cerebral tissue extraction. It also provides some manual editing features that were used to remove the cerebellum and brain stem (since we are only interested in the cerebral cortex). We note that further automation may be possible, using the methods proposed in [6], [23], and [24] but, in our experience, some manual intervention was always required, even with these approaches. Fig. 3 shows the three slices from Fig. 2 after this procedure was applied. The increased contrast apparent in these images is simply the result of image intensity rescaling.

The final step in preprocessing is to trilinearly interpolate the segmented volume to cubic voxels having the in-plane resolution in all three directions. This reduces the directional dependency in subsequent processing.

B. Fuzzy Segmentation of GM, WM, and CSF

There has been a trend in the recent literature favoring the use of fuzzy segmentations over hard segmentations in defining anatomical structures [25]. Fuzzy segmentations retain more information from the original image than hard segmentations by taking into account the possibility that more than one tissue class may be present in a single voxel. This circumstance often occurs when imaging very fine structures, resulting in partial volume averaging. Small errors in the data acquisition or segmentation will also be less of a factor in fuzzy segmentations since this will only alter the segmentation by some fractional number while in a hard segmentation, small errors might change the entire classification of a voxel.
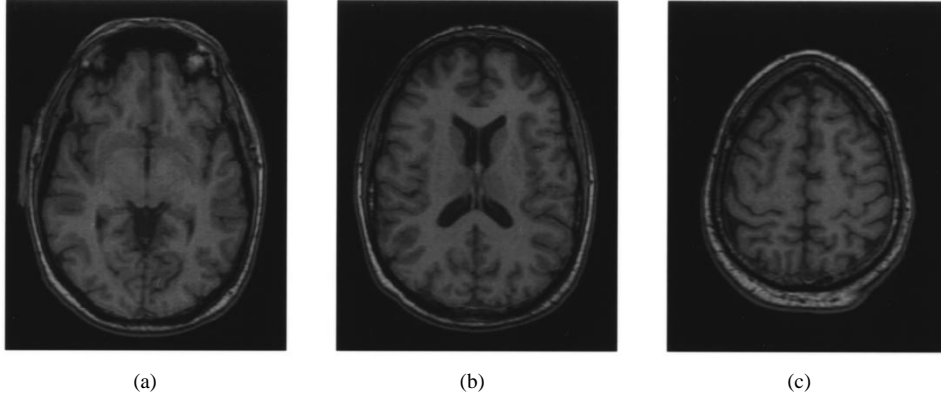
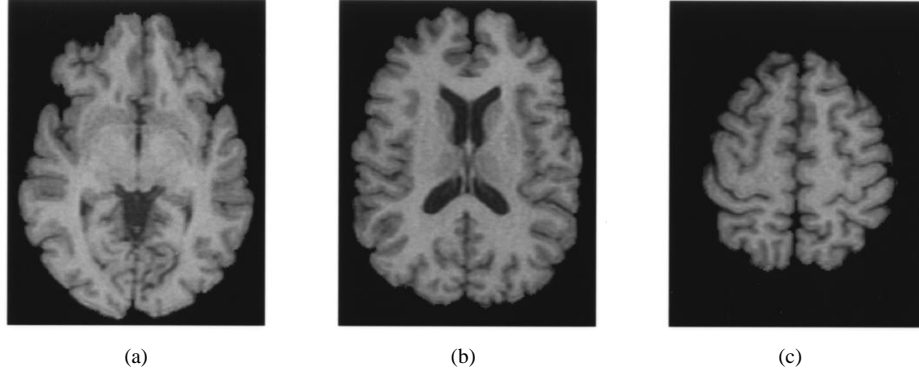Fig. 2. Sample slices from acquired MRI data set.

Fig. 3. Sample slices after the cerebral tissue extraction.

MR images sometimes suffer from intensity inhomogeneities caused predominantly by nonuniformities in the RF field during acquisition [26], [27]. The result is a slowly varying shading artifact appearing across the image that can produce errors in intensity-based segmentation methods. In particular, this artifact may cause the position of the reconstructed cortex in various regions of the brain to be shifted slightly from its true position. Robustness to intensity inhomogeneities is therefore an important requirement in a cortical surface reconstruction algorithm.

Recently, we reported a new method called adaptive fuzzy c-means (AFCM) [28] to obtain fuzzy segmentations of 2-D MR images that are robust to intensity inhomogeneities. AFCM iteratively estimates the fuzzy membership functions for each tissue class, the mean intensities (called centroids) of each class, and the inhomogeneity of the image, modeled as a smoothly varying gain field. The fuzzy membership functions, constrained to be between zero and one, reflect the degree of similarity between the observed voxel intensity and the centroid of that tissue class. Unlike several other well-known methods for inhomogeneity correction [27], [29], AFCM is an unsupervised algorithm. Thus, it does not require any training data or other manually selected data. Our comparisons have also shown that AFCM provides more accurate segmentations than several other competing unsupervised methods [30]. We now briefly describe the steps of AFCM for 3-D images. Details of its derivation for 2-D images are provided in [28].

Let $y(\boldsymbol{x})$ be the observed image intensity at voxel $\boldsymbol{x}$, $u_k(\boldsymbol{x})$ be the membership value at $\boldsymbol{x}$ for class k such that $u_k(\boldsymbol{x}) \geq 0$ and $\Sigma_{k=1}^{K} u_k(\boldsymbol{x}) = 1$, c_k be the centroid of class k, and $g(\boldsymbol{x})$ be the unknown gain field to be estimated. K, the total number of classes, is assumed to be three, corresponding to GM, WM, and CSF. Background pixels are ignored. The steps for AFCM are as follows.

1) Initial values for centroids, $c_k, k = 1, \cdots, K$, are selected automatically, as described in [31], and the gain field $g(\boldsymbol{x})$ is set to one for all $\boldsymbol{x}$.

2) Compute memberships as follows:

$$u_k(\boldsymbol{x}) = \frac{\|y(\boldsymbol{x}) - g(\boldsymbol{x})c_k\|^{-2}}{\displaystyle\sum_{l=1}^{K} \|y(\boldsymbol{x}) - g(\boldsymbol{x})c_l\|^{-2}} \qquad (1)$$

for all $\boldsymbol{x}$ and $k = 1, \cdots, K$.

3) Compute new centroids as follows:

$$c_k = \frac{\displaystyle\sum_{\boldsymbol{x}} u_k^2(\boldsymbol{x})g(\boldsymbol{x})y(\boldsymbol{x})}{\displaystyle\sum_{\boldsymbol{x}} u_k^2(\boldsymbol{x})g^2(\boldsymbol{x})}, \qquad k = 1, \cdots, K. \quad (2)$$

4) Compute new gain field by solving the following space-varying difference equation for $g(\boldsymbol{x})$:

$$y(\boldsymbol{x}) \sum_{k=1}^{K} u_k^2(\boldsymbol{x})c_k = g(\boldsymbol{x}) \sum_{k=1}^{K} u_k^2(\boldsymbol{x})c_k^2$$
$$+ \lambda_1(g(\boldsymbol{x}) * H_1(\boldsymbol{x})) + \lambda_2(g(\boldsymbol{x}) * H_2(\boldsymbol{x})) \quad (3)$$
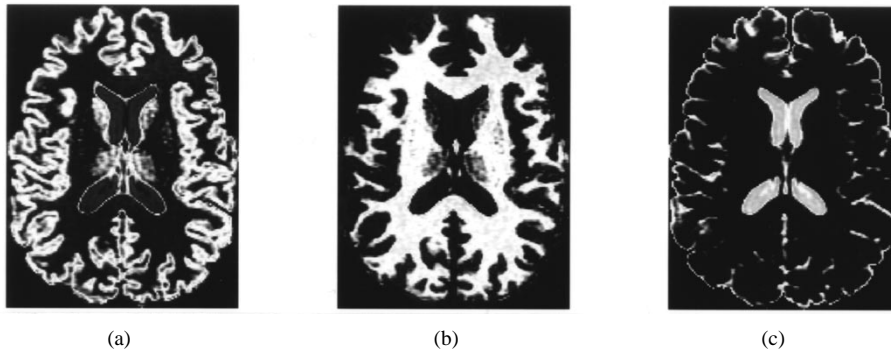
Fig. 4.   Sample slice from membership functions computed using AFCM. (a) GM. (b) WM. (c) CSF.
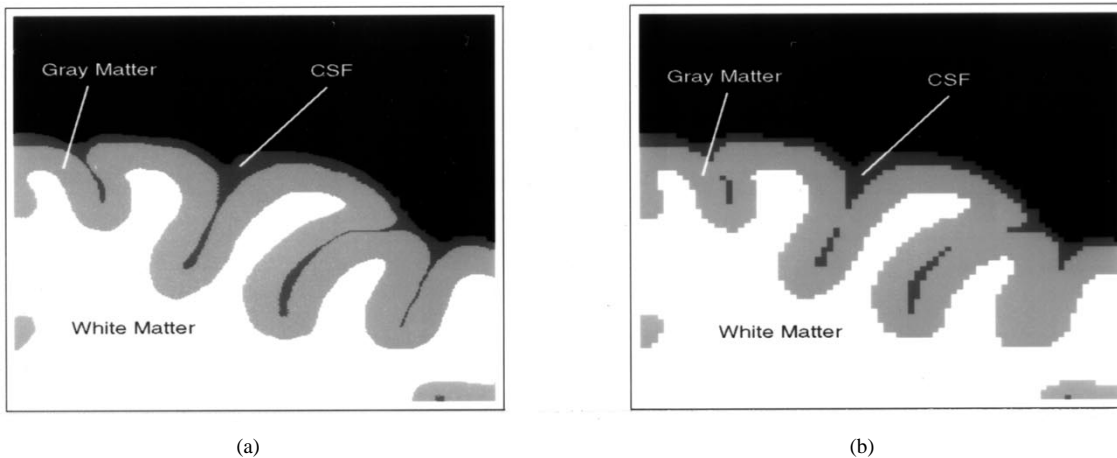

Fig. 5.   Resolution problems in determining the cortical surface. (a) Ideal image. (b) Sampled image.

where $H_1(\boldsymbol{x}) = d_x * \check{d}_x + d_y * \check{d}_y + d_z * \check{d}_z$ and $H_2(\boldsymbol{x}) = d_{xx} * \check{d}_{xx} + d_{yy} * \check{d}_{yy} + d_{zz} * \check{d}_{zz} + 2(d_{xy} * d_{xy}) + 2(d_{yz} * d_{yz})$. The operators $d_x, d_y,\ d_z$ are finite differences along the axes of the image volume and $d_{xx} = d_x * d_x$, $d_{yy} = d_y * d_y, d_{zz} = d_z * d_z$, $d_{xy} = d_x * d_y$, and $d_{xz} = d_x * d_z$ are second-order finite differences. Here we have used the notation $\check{f}(i) = f(-i)$. The symbol $*$ denotes the discrete convolution operator.

5) If the algorithm has converged, then quit. Otherwise, go to Step 2.

Convergence is defined as when the maximum change in the membership functions over all pixels between iterations is less than 0.01. In Step 4 of the algorithm, λ_1 and λ_2 are parameters that control the expected smoothness of the inhomogeneity. These parameters were determined empirically and have demonstrated robustness to inaccurate selection. The gain field $g(\boldsymbol{x})$ in Step 4 was computed using a multigrid algorithm (see [28]). A typical result from AFCM is shown in Fig. 4.

C. Estimation of Initial Surface with the Correct Topology

In order to use a deformable surface model to accurately reconstruct the extremely convoluted cortical surface, a good initial surface is required. In the past, deformable surfaces have been typically initialized using simple geometric objects (e.g., a sphere or ellipsoid) outside the cortical surface or by manual interaction [15], [6], [13], [16]. When initialized from

outside the cortical surface, however, deformable surfaces have difficulty progressing into the sulci [16]. As shown in Fig. 5, the primary difficulty with this approach is that sulci can be narrow, relative to the resolution of the scanner, so that the imaged sulci become connected [9]. As a result, these deformable surfaces produce cortical surface reconstructions that lack deep folds. Manual initializations yield better results, but they are labor intensive and time consuming for 3-D data sets.

Because of the presence of WM, there is more space between the cortical folds on the inside of the cortex than there is on the outside (see Fig. 5). Therefore, initializing the deformable surface on the inside of the cortex is a promising strategy [1], [20], [10]. Ideally, we desire an initial surface that is on the inside of the cortex, is close to the final surface, and has the correct topology: that of a sphere.[1] As shown in Fig. 5, the GM/WM interface is both inside and close to the cortex. Our approach is to find a surface that approximates the GM/WM interface by finding an isosurface of a filtered WM membership function. Filtering is required in order to make the initial surface have the correct topology. We now describe this approach in detail.

1) Using an Isosurface Algorithm: An isosurface is a surface that passes through all locations in space where a continuous data volume is equal to a constant value. The construction of isosurfaces is a well-studied problem [8], [32], [33]. The result of a typical isosurface algorithm usually consists of

---

[1] The cerebral cortex actually has a hole at the brain stem. Here, we reconstruct a closed surface that passes through the brain stem.

triangle meshes that are discrete representations of the corresponding continuous isosurfaces.

Since voxels at the GM/WM interface contain both GM and WM, an isosurface can be computed on the WM membership function obtained from AFCM, to yield an estimate of the GM/WM interface. In order to use isosurfaces in the context of our work, several issues need to be addressed.

- *Extraneous connected structures*: The boundaries of the hippocampus, the ventricles, and the putamen are generally connected with the cortical GM/WM interface in the WM membership function. This may cause isosurfaces computed from the WM membership function to be a composite of the cortical GM/WM interface and these extraneous connected surfaces. Since we are only interested in reconstructing the cortical GM/WM interface, we manually remove the hippocampal formation and fill both the ventricles and the putamen in the WM membership function. This process is facilitated with the aid of region-growing algorithms and takes only a small portion of the total processing time.
- *Mesh selection*: The output from an isosurface algorithm on the WM membership function usually contains multiple meshes. Since these meshes are physically disconnected from each other, they can be distinguished from one another by their vertex connectivity. Among all these meshes, the one with the largest number of vertices corresponds to the GM/WM interface.
- *Topology*: Isosurfaces are, in general, topologically unconstrained. We assume that the topology of the GM/WM interface is equivalent to that of a sphere. However, imaging noise often induces the formation of small handles (like that of a coffee cup) on the computed WM isosurface. These small handles are inconsistent with the assumed anatomical topology and special care is required in order to obtain an initial surface with the correct topology.

2) Correcting Surface Topology: The existence of handles in a surface can be detected by computing the surface's Euler characteristic, χ [34]. For a closed surface, χ can only assume an integer value less than or equal to two. A surface is topologically equivalent to a sphere when $\chi = 2$. The existence of handles in the surface reduces the value of χ by two for each handle.

The Euler characteristic can be computed from a triangulation of the surface by [35]

$$\chi = V - E + F \tag{4}$$

where V is the number of vertices, E is the number of edges, and F is the number of faces. The Euler characteristic is a topological invariant of a surface and does not depend on the method of triangulation.

We found that the handles on the surface can be eliminated by successively median filtering the WM membership function and recomputing its isosurface until the largest isosurface triangle mesh has $\chi = 2$. The resulting surface is a smoothed approximation to the GM/WM interface and has the topology of a sphere.

TABLE I
SIZE AND EULER CHARACTERISTICS OF MESHES
FROM THE ORIGINAL ISOSURFACE CALCULATION

No. of vertices	χ	No. of meshes
360,104	−1010	1
506	−6	1
250 − 499	2	1
100 − 249	2	11
50 − 99	2	28
25 − 49	2	97
6 − 24	2	1970

TABLE II
EULER CHARACTERISTIC OF LARGEST
RESULTING SURFACE AFTER EACH ITERATION

No. of iterations	χ
0	−1010
1	−56
2	−14
3	−4
4 − 7	−2
8	0
9	2

3) Summary of Surface Initialization: Our procedure for computing an initial estimate of the cortical surface with the correct topology can be summarized as follows.

1) Manually remove the hippocampal formation and fill both the ventricles and the putamen in the WM membership function.
2) Compute an isosurface on the preprocessed WM membership function at the value 0.5.
3) Extract only the connected surface with the largest number of vertices.
4) Compute the Euler characteristic χ of the extracted surface.
5) If χ is not equal to two, then apply a $3 \times 3 \times 3$ median filter to the preprocessed WM membership function, recompute the isosurface on the filtered data, and go to Step 3.

Isosurfaces were generated using the IBM Visualization Data Explorer software which uses the ALLIGATOR algorithm [33].[2] Except for Step 1, all of the steps are performed automatically.

A typical result of applying the above procedure to one of our data sets is shown in Tables I and II, and Fig. 6. Table I shows the number of meshes and their χ values before any median filtering has taken place. The one mesh that is clearly much larger than all other meshes represents an estimate of the GM/WM interface with an incorrect topology. Table II shows how the χ of the largest resulting mesh is increasing with each iteration and eventually converges to the desired value of two. Although there is no theoretical proof that successive median filtering will cause the Euler characteristic to converge to two, we have found empirically that this is the

[2]This implementation of the ALLIGATOR algorithm sometimes results in isosurfaces that contain singular points where two different parts of the mesh meet at one vertex, which ALLIGATOR should prohibit. In this case, methods to remove singular points automatically were also incorporated into the iterative procedure.
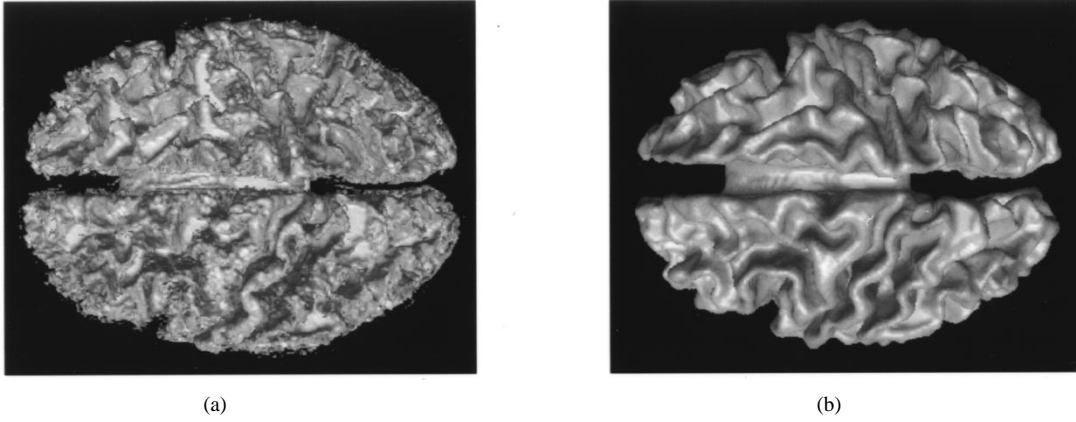
Fig. 6.   (a) Isosurface of WM membership function with the incorrect topology. (b) Estimated initial surface with the correct topology.

case. Additional results on the convergence of the deformable surface initialization are provided in Section III-B1.

Fig. 6(a) shows the result of the isosurface algorithm on the original WM membership function at a value of 0.5. Multiple meshes and topological inconsistencies are present. Fig. 6(b) shows the final topologically correct mesh after nine iterations of our procedure. We see that although we have not yet applied the deformable surface model, many of the prominent geometrical characteristics of this cortical surface are already apparent.

D. Refinement of the Initial Surface Using a Deformable Surface Model

After obtaining an initial estimate of the cortical surface that is topologically correct, the surface requires refinement. Because of median filtering, the initial surface in the previous step is a smoothed version of the GM/WM interface. Using deformable surfaces, it is possible to have this initial surface move toward the central layer of the GM. The main problem here lies in defining the external forces. Below, we first give a brief overview of deformable surface models and then describe our specific model, which uses external forces that push the initial surface toward the central layer of the GM. For a thorough survey on deformable surface models, we refer readers to the survey paper by McInerney and Terzopoulos [36].

1) Deformable Surface Models: The traditional deformable surface is a parameterized surface $\boldsymbol{x}(\boldsymbol{u}) = [x(\boldsymbol{u}), y(\boldsymbol{u}), z(\boldsymbol{u})]^T$, $\boldsymbol{u} = (u^1, u^2) \in [0, 1] \times [0, 1]$ that moves through the spatial domain of a three-dimensional (3-D) image to minimize an energy functional [36]–[38]. A typical example of such an energy functional is

$$E = \int \tfrac{1}{2} \left(w_1 \sum_{i=1}^{2} |\boldsymbol{x}_i|^2 + w_2 \sum_{i,j=1}^{2} |\boldsymbol{x}_{ij}|^2 \right) + E_{\text{ext}}(\boldsymbol{x}) \, d\boldsymbol{u} \tag{5}$$

where w_1 and w_2 are weighting parameters that control the surface's tension and rigidity, $\boldsymbol{x}_i$ and $\boldsymbol{x}_{ij}$ denote the first and second partial derivatives of $\boldsymbol{x}$ with respect to u^i and $E_{\text{ext}}(\boldsymbol{x})$ is the external energy function derived from the image. It can be shown that the deformable surface minimizing the above energy functional can be obtained by finding the steady-state

solution of the following dynamic equation:

$$\boldsymbol{x}_t = \boldsymbol{F}_{\text{int}} + \boldsymbol{F}_{\text{ext}} \tag{6}$$

where the internal forces are given by $\boldsymbol{F}_{\text{int}} = w_1 \nabla_{\boldsymbol{u}}^2 \boldsymbol{x} - w_2 \nabla_{\boldsymbol{u}}^2 (\nabla_{\boldsymbol{u}}^2 \boldsymbol{x})$ and the external forces are given by $\boldsymbol{F}_{\text{ext}} = -\nabla E_{\text{ext}}(\boldsymbol{x})$. The symbol $\nabla_{\boldsymbol{u}}^2 = (\partial^2/(\partial u^1)^2) + (\partial^2/(\partial u^2)^2)$ is the Laplacian operator defined in the parameter space. Note that in (6), an auxiliary variable time t is introduced to make deformable surface $\boldsymbol{x}$ dynamic.

2) External Forces: Traditional deformable surface models typically use external force fields that are conservative vector fields since they are computed from the spatial gradient of a scalar function. The scalar function is usually either the magnitude of the image intensity gradient or a distance function derived from an analysis of the objects within the image [37], [39]. Such deformable surface models, however, have difficulty progressing into boundary concavities [18] which, in our case, are the gyri of the cortical GM. We recently reported a new external force model, called gradient vector flow (GVF) [18], [40], and, even more recently, an extension to GVF called generalized gradient vector flow (GGVF) [41], each of which can be used to address this problem. The external forces we use in this paper combine GGVF with a constrained pressure force which further improves overall convergence of the deformable surface. We now briefly describe this new external force model.

A GGVF field $\boldsymbol{v}(\boldsymbol{x})$ where $\boldsymbol{x} = (x, y, z) \in \boldsymbol{R}^3$ is defined as the equilibrium solution of the following system of partial differential equations:

$$\boldsymbol{v}_t = g(|\nabla f|) \nabla^2 \boldsymbol{v} - h(|\nabla f|)(\boldsymbol{v} - \nabla f) \tag{7a}$$
$$\boldsymbol{v}(\boldsymbol{x}; 0) = \nabla f \tag{7b}$$

where $\boldsymbol{v}_t$ denotes the partial derivative of $\boldsymbol{v}(\boldsymbol{x}; t)$ with respect to t and $\nabla^2 = (\partial^2/\partial x^2) + (\partial^2/\partial y^2) + (\partial^2/\partial z^2)$ is the Laplacian operator (applied to each spatial component of $\boldsymbol{v}$ separately). In this work, we set f to be the GM membership function and $g(r) = \exp\{-(r/\kappa)^2\}$ and $h(r) = 1 - g(r)$ where κ is a scalar and r is a dummy variable. We note that if $g(r) = \mu$ and $h(r) = r^2$ where μ is a positive scalar, GGVF reduces to GVF. The advantage in using $g(r)$ and $h(r)$ as defined here is that it leads to improved convergence properties for narrow boundary concavities [41].
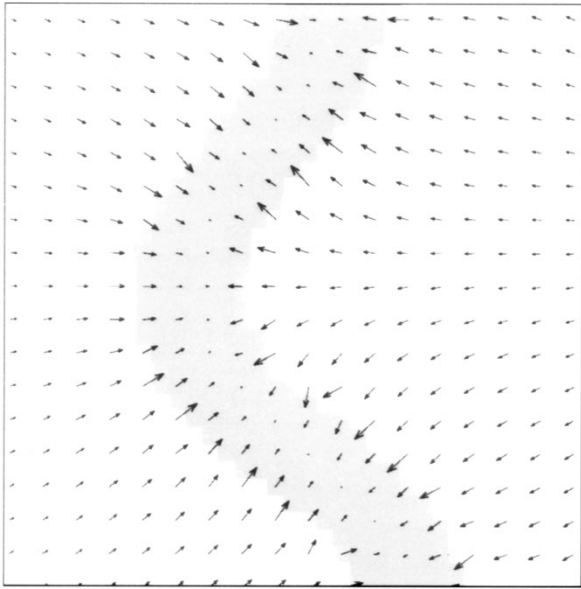
Fig. 7. GGVF vector field converges to the center of a thick edge.

Fig. 8. Initial deformable contour shown in black and final converged deformable contour shown in white.

When applied to a thick sheet such as the cortex, GGVF, through its diffusion process, creates forces that point to the central layer of the cortex [42]. To illustrate this, in Fig. 7 we show a 2-D example of GGVF applied to a ribbon. The figure shows GGVF force vectors clearly pointing toward the central layer of the ribbon from which they were calculated.

Despite the improved convergence properties of GGVF over conventional external forces, deformable surface convergence can be slow and the surface still may not fully capture the gyri in some areas of the cortex. Thus, we combine GGVF with pressure forces [43], [39] that are constrained to operate only on parts of the surface that are not within the GM. This constraint, similar to that in [23], helps increase the speed of convergence of the deformable surface when it is far from the GM and improves the fidelity of the final result when it is within the GM. The resulting external force is given by

$$F_{\text{ext}}(\boldsymbol{x}) = w_3\langle \boldsymbol{v}(\boldsymbol{x}), \boldsymbol{n}(\boldsymbol{x})\rangle\boldsymbol{n}(\boldsymbol{x}) + w_4 C(\boldsymbol{x})\boldsymbol{n}(\boldsymbol{x}) \qquad (8)$$

where w_3 and w_4 are weights, $\boldsymbol{v}(\boldsymbol{x})$ is the GGVF field, $\boldsymbol{n}(\boldsymbol{x})$ is the outward unit normal vector of the surface at $\boldsymbol{x}$, $\langle\cdot,\cdot\rangle$ is the inner product of two vectors, and $C(\boldsymbol{x})$ is a constraint field (defined below). Since the component of the external force in the tangent plane will affect the parameterization of the surface but not its shape, we project $\boldsymbol{v}(\boldsymbol{x})$ onto the normal direction at surface position $\boldsymbol{x}$. The internal force is therefore solely responsible for controlling the surface parameterization, while the external force is solely responsible for deforming the surface toward the feature of interest.

The constrained pressure force $C(\boldsymbol{x})\boldsymbol{n}(\boldsymbol{x})$ is designed to push the surface outward only until it enters the GM, whereupon the pressure force then turns off. To accomplish this, we define the strength of the pressure force, as controlled by the constraint field $C(\boldsymbol{x})$, to be

$$C(\boldsymbol{x}) = \begin{cases} 0, & \text{if } |2u_{wm}(\boldsymbol{x}) + u_{gm}(\boldsymbol{x}) - 1| < \delta \\ 2u_{wm}(\boldsymbol{x}) + u_{gm}(\boldsymbol{x}) - 1, & \text{otherwise.} \end{cases}$$
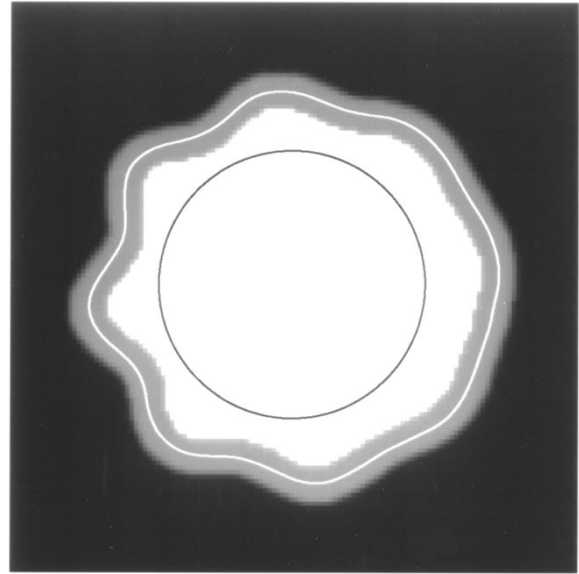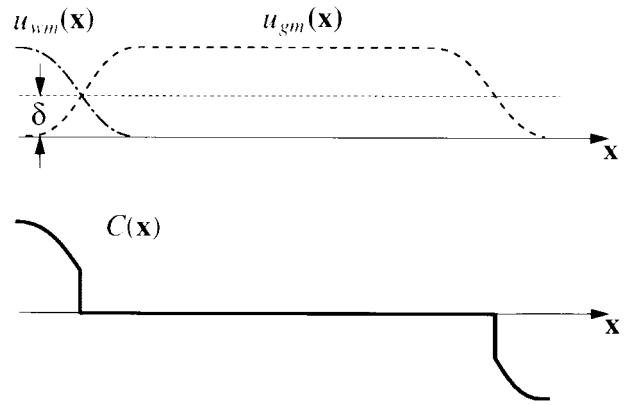
Fig. 9. Illustration of behavior of $C(\boldsymbol{x})$.

where $u_{wm}(\boldsymbol{x})$ and $u_{gm}(\boldsymbol{x})$ are the WM and GM membership functions. Here, δ is a threshold that controls the width of the GM region where the pressure force is disabled, i.e., $C(\boldsymbol{x}) = 0$. In our experiments we used $\delta = 0.5$. The behavior of $C(\boldsymbol{x})$ is illustrated in Fig. 9 where one-dimensional (1-D) profiles of GM and WM membership functions and the corresponding $C(\boldsymbol{x})$ are plotted. It is easy to see that when $\boldsymbol{x}$ is in the WM $C(\boldsymbol{x})$ is positive, which would cause the pressure force to push a deformable surface toward the GM. When $\boldsymbol{x}$ is in the GM $C(\boldsymbol{x})$ is zero and the GGVF force is the only external force. When $\boldsymbol{x}$ is outside the GM in the CSF or background $C(\boldsymbol{x})$ is negative, causing the pressure force to push the deformable surface back toward the GM.

To demonstrate the behavior of these external forces, we applied a 2-D deformable contour, a 2-D analog to deformable surfaces in 3-D, using the external forces defined in (8) to the computer phantom shown in Fig. 8. Here, the gray ribbon is analogous to the cortical GM, sandwiched between the WM and the CSF. In the figure, the initial deformable contour is the circle shown in black, while the final converged contour
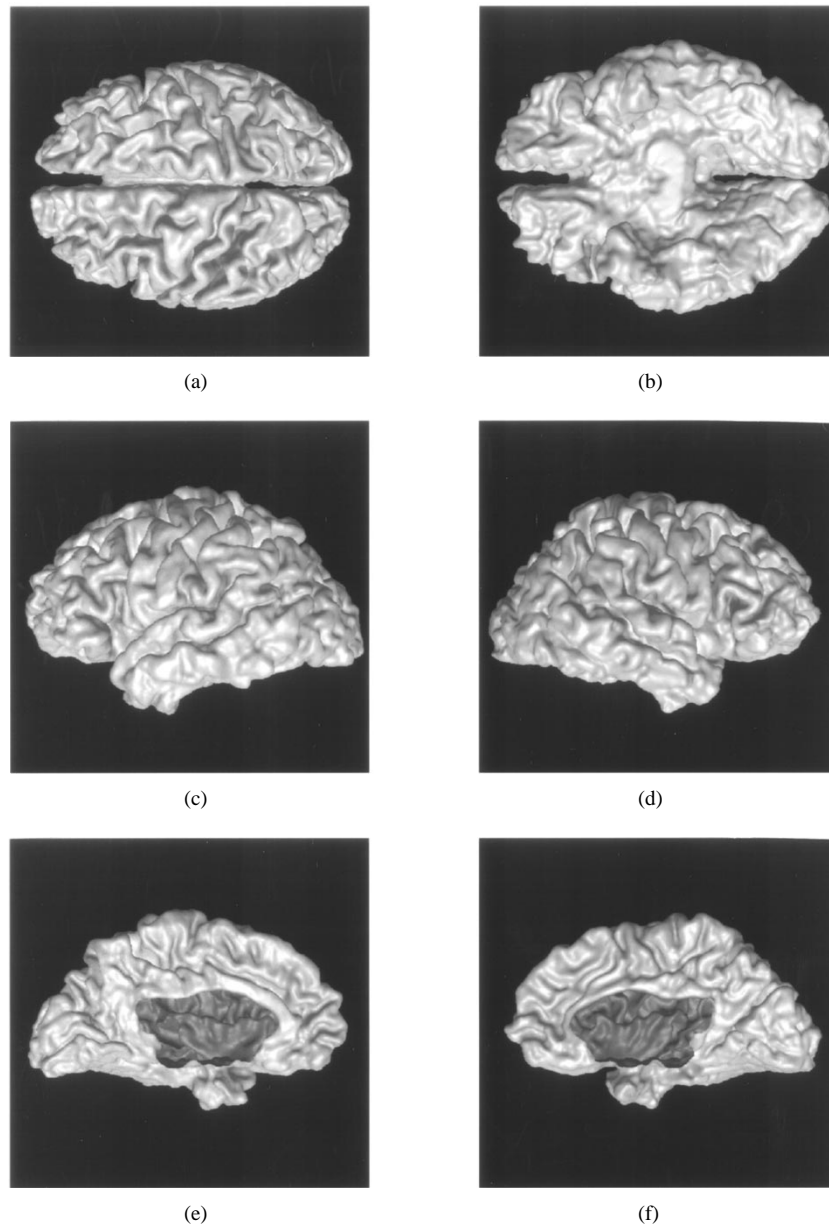
Fig. 10. Surface renderings of a reconstructed cortical surface from one subject displayed from multiple views. (a) Top. (b) Bottom. (c) Left. (d) Right. (e) Left medial. (f) Right medial.

is shown in white. We note that the final contour rests on the center of the simulated GM.

3) Adaptive Parameters: Because of image noise, relatively large internal forces are desirable where the deformable surface is far from the GM. Large internal forces cause the deformable surface to be very smooth, however, and prevent the surface from accurately conforming to the central cortical layer. Therefore, lower internal forces are desirable where the deformable surface lies within the GM. We achieve this by allowing w_1 and w_2 to be spatially varying parameters in (5) with respect to the strength of the constraint field $C(\boldsymbol{x})$ as follows:

$$w_i(\boldsymbol{x}) = \begin{cases} w_i, & \text{if } |C(\boldsymbol{x})| = 0 \\ \alpha_i w_i, & \text{otherwise} \end{cases}$$

for $i = 1, 2$, where $\alpha_i \geq 1$.

E. Reconstructed Surface

We have implemented the proposed deformable surface based on a simplex mesh representation of the underlying continuous surface [44]. Simplex meshes can be easily obtained by applying a dual operation to the triangle meshes generated by the isosurface algorithm. Details of our deformable surface implementation can be found in [42]. As an example, we carried out the complete surface reconstruction on the sample data set appearing in Figs. 2–4, and 6. Different views of the reconstructed surface are shown in Fig. 10, and crosssectional views are shown in Fig. 11. The parameters used to achieve this result are $\lambda_1 = 2 \times 10^4$ and $\lambda_2 = 2 \times 10^5$ for AFCM; $\kappa = 0.2$ for GGVF; and $w_1 = 0.25$, $w_2 = 0$, $w_3 = 0.5$, $w_4 = 0.01$, $\alpha_1 = 3$, and $\alpha_2 = 0$ for the deformable surface. While this may appear to be a large number of parameters to tune, we have found that they are fairly robust to both changes
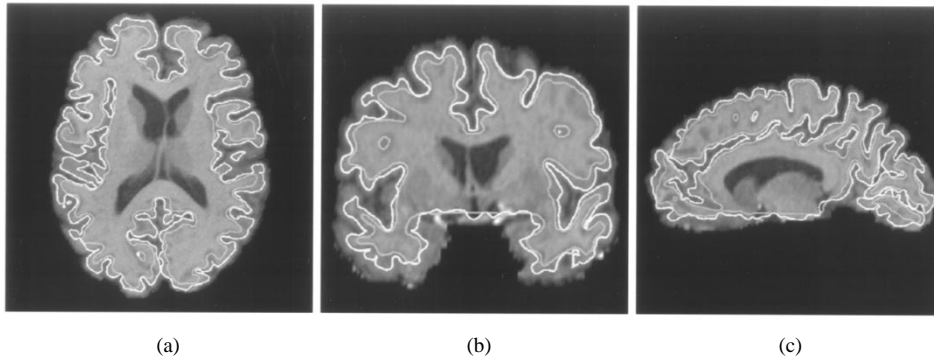
Fig. 11. Cross-sectional views of the reconstructed cortical surface (in white) and the initial surface (in gray). (a) Axial. (b) Coronal. (c) Sagittal.

in their values and the data. In fact, all the results presented in the following section use these same parameters.

At first glance, the sulci in the surface shown in Fig. 10 appear too open and do not resemble those from a normal brain. Note, however, that this reconstruction represents the central layer of the cortical GM, an object that we are not accustomed to viewing. The central layer is not the brain's outer surface, as would be seen from a cadaver brain or a standard isosurface reconstruction of the cortical surface. Careful inspection reveals exquisite depiction of the major sulci, including the central sulcus, superior temporal sulcus, calcarine sulcus, parieto-occipital sulcus, and the Sylvian fissure. Secondary sulci such as the pre- and postcentral sulci, the superior frontal sulcus, and the cingulate sulcus are also readily discernible. Their prominence in these pictures is, to some extent, because we are depicting a more open brain surface, but also because the central cortical layer is the most natural representation of the overall geometry of the cortex. We note that the small area of cortical surface passing through the brain stem region is not cortical gray matter, but it is necessary to generate a closed surface.

The crosssectional pictures in Fig. 11 show how the reconstructed surface tracks the central cortical layer over the entire cortex, including its deepest folds. In fact, because the surface is initialized inside the cortex, the most difficult areas to reconstruct are typically the gyri, not the sulci. A typically difficult area is the superior temporal gyrus, which is not particularly well reconstructed on the left side of the picture in Fig. 11(b). Other features of interest appearing on these crosssections are the various islands of apparently disconnected surface intersections. These features, however, are actually parts of the surface protruding through the image plane. The surface being portrayed is simply connected with the topology of a sphere.

III. RESULTS

We applied the described cortical surface reconstruction method to MR brain images from six subjects, four of which were taken from the Baltimore Longitudinal Study on Aging [45]. The same parameters used in the example from the previous section were used for these six studies. Using an SGI O2 workstation with a 174-MHz R10000 processor, the total processing time per study varied between 4.5 and 6 h. The time required for manual interaction varied between 0.5 h and

1 h for a trained operator and AFCM required approximately 1 h. The automated steps in GM/WM interface estimation take approximately 0.5 h and produce a mesh with between 200 000 and 400 000 vertices. Because of the large number of vertices in the mesh, it takes the deformable surface algorithm about 3 h to produce the final reconstructed surface. Note that both AFCM and the deformable surface algorithms are fully automated steps.

A. Qualitative Results

Fig. 12 shows the right medial surface of each of the six reconstructed cortical surfaces. Prominent sulci include the calcarine sulcus, the parieto-occipital sulcus, and the cingulate sulcus. Fig. 13 shows a coronal view of a slice taken approximately at the anterior commissure of each reconstructed cortical surface. These figures show that the surfaces reside on the central cortical layer and that buried gyri (such as the insula) are found. Although most gyri are properly depicted, certain regions, such as the superior temporal gyrus, are sometimes not found accurately. This is particularly apparent in Fig. 13(e) and (f). We are considering further improvements to correct these deficiencies.

B. Quantitative Results

Several quantitative validation experiments were performed to evaluate the robustness and accuracy of our surface reconstruction approach. These are described in this section.

1) Initialization Algorithm Validation: Application of our method to multiple subjects allowed a preliminary validation of the convergence of the deformable surface initialization algorithm (see Section II-C). The results are shown in Table III, where we observe that the median filter used in the iterative process effectively eliminates handles on the surfaces and that in all six cases, the Euler characteristic of the surface converged to two in fewer than ten iterations.

2) Gray Matter Percentage: Since our deformable surface algorithm is designed to converge to the GM, as an initial evaluation for each reconstructed surface we computed the percentage η of the surface area that was inside the GM

$$\eta = \frac{\int_{\Omega} H_{gm}(\boldsymbol{x}) dA}{\int_{\Omega} dA} \times 100$$
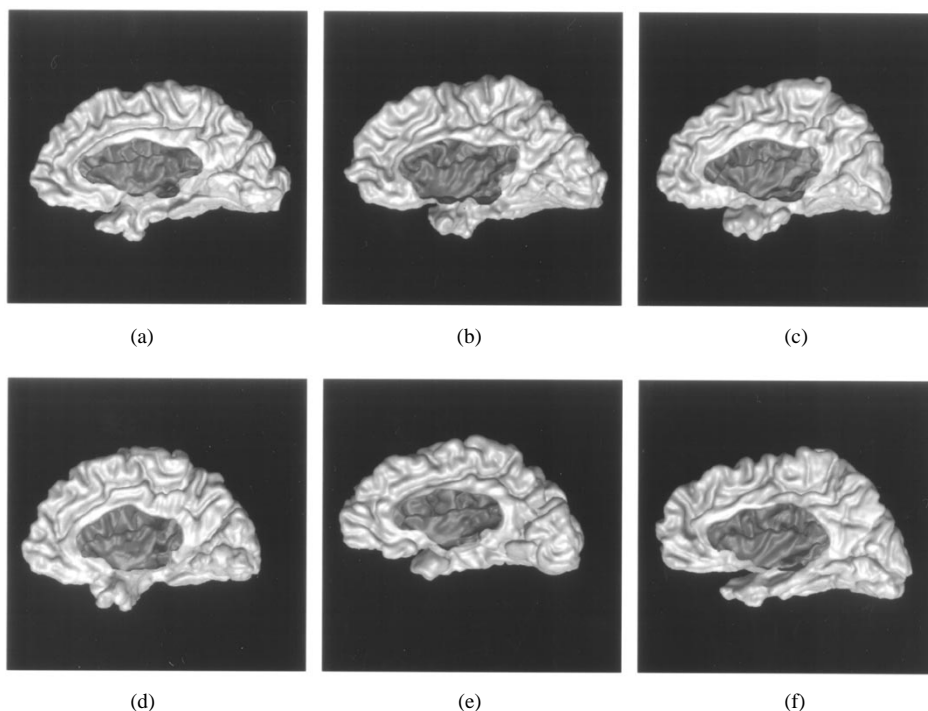
Fig. 12.   The medial view of surface renderings of all six reconstructed cortical surfaces (subjects 1–6 displayed from left to right and top to bottom).
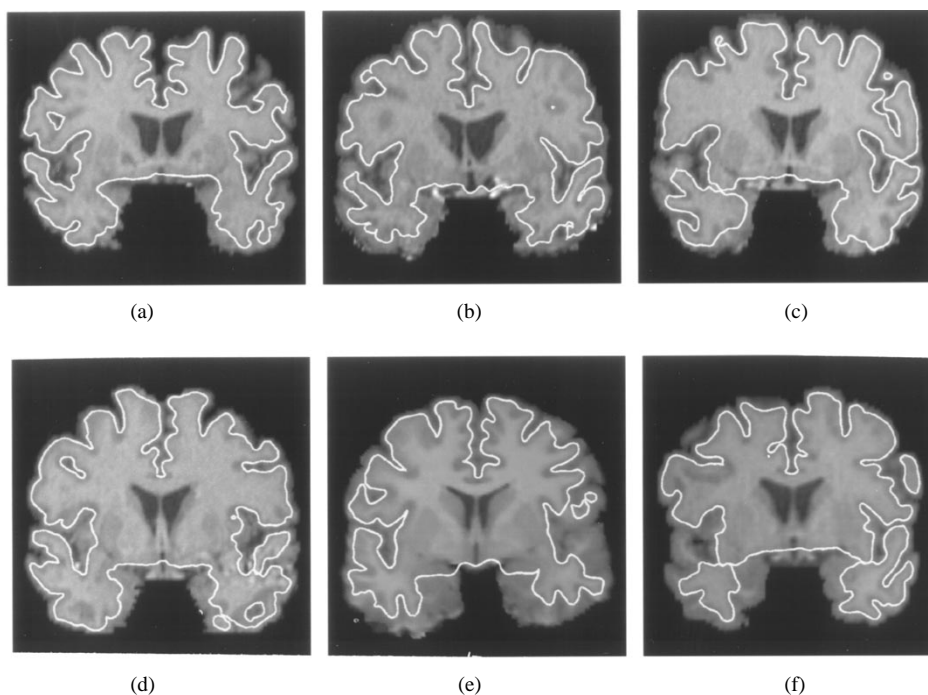

Fig. 13.   From left to right and top to bottom, the coronal slice across the anterior commissure for subjects 1–6 superimposed with the crosssection of the corresponding reconstructed cortical surface.

where Ω is the reconstructed surface with the brain-stem region excluded and H_{gm} is a binary segmentation of GM. H_{gm} is derived from the fuzzy membership functions as follows:

$$H_{gm}(\boldsymbol{x})$$
$$= \begin{cases} 1, & \text{if } u_{gm}(\boldsymbol{x}) = \max(u_{csf}(\boldsymbol{x}), u_{gm}(\boldsymbol{x}), u_{wm}(\boldsymbol{x})) \\ 0, & \text{otherwise.} \end{cases}$$

The GM percentage for each reconstructed cortical surface is shown in Table IV. All the reconstructions have GM percentage over 96%. We believe that those parts of the surface not lying in the GM are mostly found in the WM crossing a gyrus that is not reconstructed well, such as the superior temporal gyrus.

3) Landmark Errors: A high GM percentage is a necessary condition for the reconstructed surface to be accurate because
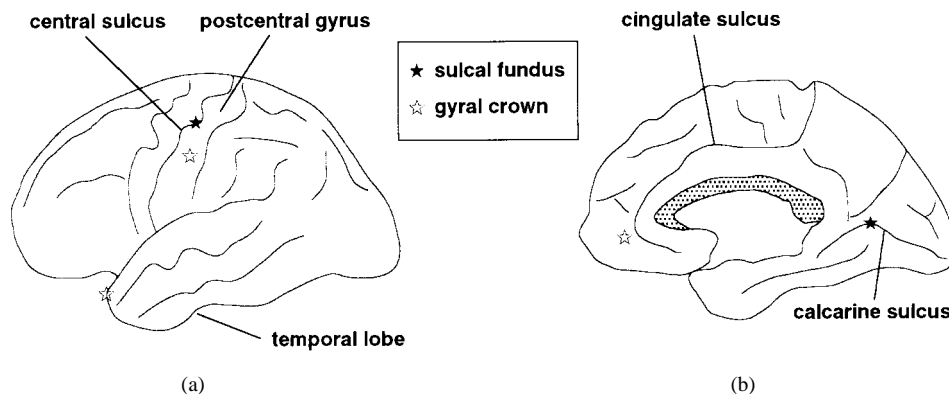
Fig. 14. Illustration of landmark locations. (a) Lateral view. (b) Medial view.

TABLE III
EULER CHARACTERISTICS OF SURFACES GENERATED
FOR SIX SUBJECTS AT DIFFERENT ITERATIONS

Iteration(s)	0	1	2	3	4	5	6	7	8	9
Subject 1	-757	-49	-6	2	--	--	--	--	--	--
Subject 2	-1010	-56	-14	-4	-2	-2	-2	-2	0	2
Subject 3	-666	-50	-16	-12	-4	-2	0	0	2	--
Subject 4	-860	-66	-24	-8	-6	-2	-2	-2	2	--
Subject 5	-253	-59	-29	-19	-13	-9	-5	-2	2	--
Subject 6	-462	-26	-12	-6	0	2	--	--	--	--

TABLE IV
GM PERCENTAGE MEASURE OF RECONSTRUCTED SURFACES FOR SIX SUBJECTS

Subject	1	2	3	4	5	6
GM%	97.97	96.92	97.31	96.74	97.64	98.45

TABLE V
LANDMARK ERRORS (IN MILLIMETERS)

Sulcus	Subject 1	2	3	4	5	6	Mean	Std
CS_1	1.21	2.40	1.48	0.22	0.63	0.47	1.10	0.80
CS_2	1.67	1.84	0.86	1.17	1.27	2.02	1.50	0.44
PCG_1	0.77	0.66	0.34	0.64	1.27	0.67	0.73	0.30
PCG_2	0.84	0.96	0.93	0.67	0.40	0.35	0.69	0.27
TLG_1	0.34	0.60	2.90	0.93	2.80	0.47	1.30	1.20
TLG_2	3.50	2.12	0.98	1.25	5.73	1.29	2.50	1.80
$CALC_1$	0.82	0.68	1.31	0.25	0.38	0.68	0.69	0.37
$CALC_2$	1.25	5.73	2.92	0.63	2.24	0.39	2.20	2.00
MFG_1	0.32	0.75	0.66	1.38	0.34	0.45	0.65	0.40
MFG_2	1.37	1.35	0.64	0.23	1.01	1.06	0.94	0.44
Mean	1.20	1.70	1.30	0.74	1.60	0.78	--	--
Std	0.91	1.60	0.91	0.43	1.70	0.53	--	--

it gives a global measure of how much of the reconstructed surface is inside the GM. The GM percentage, however, does not reflect whether the surface coincides with the central cortical layer. To get a sense of this accuracy and how it varies across the cortex, we computed a series of landmark errors for each of the six surfaces. We picked five landmarks on the central cortical layer of each hemisphere on all subjects. Fig. 14 shows the location of the landmarks picked on the brain cortex. Details of how these landmarks were picked and how the landmark errors were calculated are given in the Appendix. The landmarks were located on the fundus of the central sulcus (CS), the crown of the postcentral gyrus (PCG), the most anterior point of the temporal lobe (TLG), midway along the fundus of the calcarine sulcus (CALC), and on the medial frontal gyrus (MFG). The landmark error is defined as the minimum distance between the given landmark and the reconstructed surface.

The computed landmark errors for all six subjects are shown in Table V. Overall, the mean landmark error is between 1 and 2 mm. Many of the individual landmark errors are less than 1 mm: the size of a voxel. In particular, for landmarks located at sulcal fundi, i.e., CS and CALC landmarks, the errors are generally small since they are close to the initial deformable surface. However, there are a few exceptions where large errors are associated with these landmarks. This is because in places where the sulcal banks are very close together, our deformable surface model sometimes may travel

too far outward toward the outer brain surface. For landmarks associated with gyri, consistent small landmark errors are observed at the relatively open gyri such as the PCG and the MFG. However, for narrow extended gyri such as the TLG, the deformable surface may be stopped before reaching the correct destination, yielding larger landmark errors. In Section IV, we will discuss possible directions for further improvement.

4) Parameter Selection: Our method requires the selection of several parameters that affect its overall performance. We have found that the algorithm is quite robust to variations in λ_1, λ_2, and κ and that the nominal values we have used yield the best overall results (see [28] and [41]). Tradeoffs between the parameters controlling the deformable surface, however, can influence the result more significantly. Therefore, we conducted a numerical experiment in order to find the best ranges of parameters to use in our deformable surface model. These results are reported here.

We used the BrainWeb simulated brain data obtained from the McConnell Brain Imaging Centre at McGill University[3] [46], generated using the following parameters: 1 mm cubic voxels, T1-weighted contrast, 3% noise, and 20% inhomogeneity level. We then varied the parameters of the deformable surface model to obtain a series of reconstructed cortical surfaces. For each reconstructed cortical surface we computed its GM percentage and landmark errors. We found that the best performance occurs when $w_2 = 0$, which implies that the deformable surface has no resistance to bending. The GM

[3] http://www.bic.mni.mcgill.ca/brainweb.

TABLE VI
GM PERCENTAGE USING AFCM GM SEGMENTATION

$w_2 = 0, w_3 = 0.5$	w_4				
w_1	0	0.005	0.01	0.02	0.04
0.25	97.52	98.40	98.73	98.88	98.66
0.5	97.94	98.56	98.82	99.12	99.05
0.75	98.00	98.56	98.79	99.12	99.16

TABLE VII
GM PERCENTAGE USING TRUE GM SEGMENTATION

$w_2 = 0, w_3 = 0.5$	w_4				
w_1	0	0.005	0.01	0.02	0.04
0.25	97.53	98.32	98.59	98.72	98.54
0.5	97.87	98.45	98.67	98.93	98.87
0.75	97.91	98.40	98.64	98.94	98.97

TABLE VIII
LANDMARK ERRORS FOR PHANTOM DATA (IN MILLIMETERS)

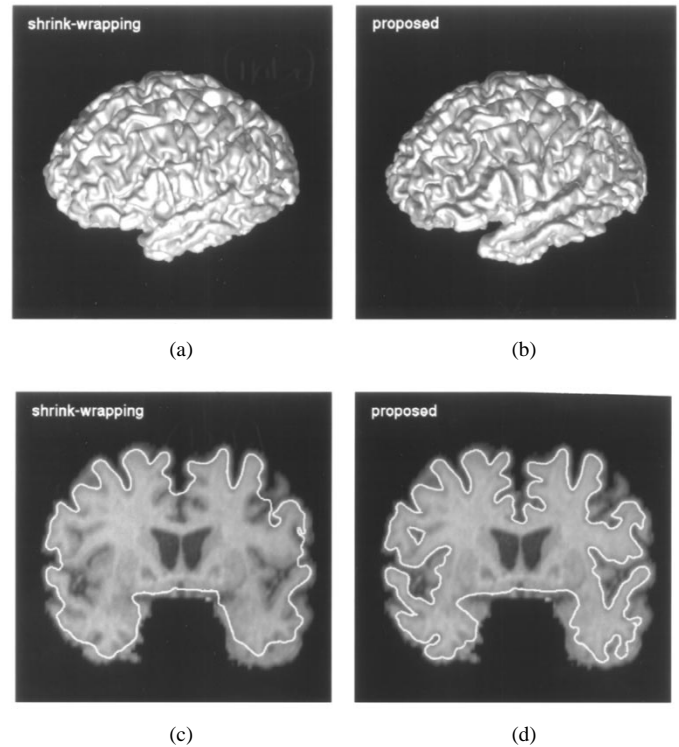| $w_3 = 0.5, w_2 = 0$	w_4				
w_1	0	0.005	0.01	0.02	0.04
0.25	0.97	0.94	0.88	0.88	0.89
0.5	1.05	0.99	0.85	0.83	0.85
0.75	1.06	1.06	0.89	0.87	0.85

Fig. 15. Surface renderings of (a) shrink-wrapping method versus (b) proposed method. Cross sections of (c) shrink-wrapping method versus (d) proposed method.

percentages computed for different w_1 and w_4 values are summarized in Table VI. From the table, $w_1 = 0.5, 0.75$ and $w_4 = 0.01, 0.02, 0.04$ seem to yield consistently higher GM percentages.

The BrainWeb simulated brain data also comes with a true GM segmentation. This allows us to compute the true GM percentage. The results are shown in Table VII. By comparing the two tables, one can see that the GM percentage computed from AFCM GM segmentation differs by at most 0.2% from the value computed from the true GM segmentation. This demonstrates the robustness of AFCM segmentation to noise and image inhomogeneities.

The landmark errors are derived from the landmarks picked on the true brain data where no noise and inhomogeneity are present. For each set of parameters, the mean of the computed landmark errors are summarized in Table VIII. From the table, $w_1 = 0.5$ and $w_4 = 0.01, 0.02, 0.04$ seem to yield consistently lower landmark errors.

The results from both GM percentages and landmark errors suggests that we achieve the lowest errors when $w_1 = 0.5$ and $w_4 = 0.01, 0.02, 0.04$. This is consistent with our conclusion through visual inspection and the parameters match well with our empirically chosen parameters.

5) Comparison with Shrink-Wrapping: Shrink-wrapping is a well-known approach to finding a parametric representation of the brain surface [15], [6], [16], [17]. This approach uses a deformable surface that is initialized as a simple geometric object (sphere or ellipsoid) outside the cortex and the surface is then pushed toward the cortex by the action of internal and external forces. For comparative purposes, we implemented a shrink-wrapping deformable model that started from an initial sphere outside the brain surface and deformed toward the central layer of the GM, using the same external forces as used in the proposed method. The proper parameters for the shrink-

wrapping deformable model are determined experimentally. The resulting surface of subject one is shown in Fig. 15(a), while the surface found by our method is shown in Fig. 15(b). These surfaces look very similar, and it is not apparent from these renderings that there is much difference in these approaches.

A profound difference between these two approaches is revealed, however, in the crosssectional images shown in Fig. 15(c) and (d). Clearly, the shrink-wrapping method only finds the outermost cortical layer. It is interesting to note that the GM percentage of the shrink-wrapping method is 94%, a fairly large number. However, this number merely indicates that the final surface resides overwhelmingly within the GM, but does not indicate how faithfully it tracks the entire cortex. In fact, the landmark errors computed for the shrink-wrapping result shows substantial errors (4–10 mm) in the CS, CALC, and MFG landmarks, which are landmarks that either reside within sulci or within the interhemispheric fissure. This demonstrates the importance of initializing the deformable surface from inside the cortical GM.

IV. DISCUSSION

We have presented a method for reconstructing cortical surfaces from MR brain images. This method combines a fuzzy segmentation method, an isosurface algorithm, and a new deformable surface model to reconstruct a surface representation of the cortical central layer. The reconstructed surfaces include deep gyri and sulci and possess the correct surface topology of the cortex. The process is largely automated and produces

surfaces that are typically within 1–2 mm of the true cortical surface.

The method for cortical surface reconstruction proposed by Dale and Sereno [1] shares several common features with the method described here. Both methods start from the GM/WM interface and use deformable surface algorithms to reconstruct the cortical surface. However, there are several major differences. In their work, image intensity inhomogeneities were not explicitly considered and no validation of their algorithm was presented. Also, they employed a 3-D floodfill algorithm to obtain the GM/WM interface but, from our experience, the floodfill algorithm can only remove holes (cavities) in the WM, but not the handles (bridges). Moreover, it is unclear what cortical layer was reconstructed by their deformable surface algorithm.

Since the proposed method generates a mapping of the entire cortical surface that preserves both deep folds and topology, various brain structures can now be studied in a more precise way. The reconstructed cortical surface can be unfolded to facilitate visualization of geometrical features [47]. Also, functional data can be mapped onto the reconstructed cortical surface to study the relationship between structure and function, especially in deep sulcal regions [48].

Future work includes further reduction of manual intervention and improved convergence of the deformable surface into narrow extended gyri. A promising way to improve the deformable surface convergence is to incorporate additional brain anatomical knowledge as demonstrated in [49] and [50]. Also, theoretical justification of applying median filtering to correct topology as well as finding improved methods for generating a topologically correct initial surface are important topics for future work.

APPENDIX
LANDMARK PICKING AND LANDMARK ERRORS

To pick landmarks, an IBM Data Explorer visual program was written to display three 2-D orthogonal views of the raw MR brain volume. Within each view, the positions of the other two slices were superimposed forming a cross. An operator then selected three views such that the center of the cross in each view lay on the central layer of the GM within a designated volume of interest (VOI). The landmark coordinates were recorded as the physical positions of these three views.

Landmarks determined in this way were treated as the truth in the calculation of landmark errors in Section III. It is important to understand the effect of operator error, however, on the reported errors. Referring to Fig. 16, we see that the picked landmark P^* will, in general, be some distance Δ from a point P on the true central layer and the reported error $e = |QP^*|$ will be different from the true error $\varepsilon = |QP|$. It is straightforward to show that $\varepsilon \in [e - \Delta, e + \Delta]$, which leads to the conclusion that e is a good measure of error provided that Δ is small relative to e. It remains to determine what is the operator error Δ.

We found that an operator can pick a point on the central layer of the cortex very accurately, using the described pro-

P : ideal landmark

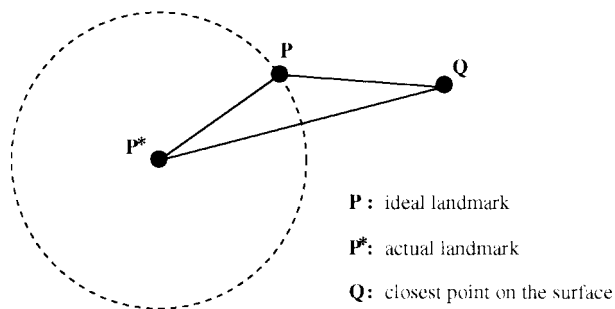P*: actual landmark

Q: closest point on the surface

Fig. 16. Illustration of the configuration of ideal landmark, actual landmark, and closest point on the surface.

cedure. The main reason for this accuracy is that the operator does not need to pick a specific point, but only a point within a VOI that is on the central cortex in all three views. To get an approximate measure of this accuracy, we designed a Monte Carlo simulation to approximate the landmark picking error introduced by the operator. We assume that our VOI is $10 \times 10 \times 10$ voxels, each voxel is 1 mm^3, and the central cortical surface in the VOI is a plane. For a plane passing through the VOI with arbitrary location and orientation, we assumed that the operator could pick the grid point closest to the plane, and the distance between this grid point and the plane is the operator error for this particular experiment. By varying the plane position and orientation randomly, we can measure the mean operator error and use it as our estimation of the landmark picking error introduced by the operator. We uniformly sampled 10^9 random planes from all possible planes passing through the VOI, yielding a mean operator error of 0.04 mm. Even if the true operator error were 2–5 times this error, it would still be relatively small in comparison to the typical errors reported in Section III.

REFERENCES

[1] A. M. Dale and M. I. Sereno, "Improved localization of cortical activity combining EEG and MEG with MRI cortical surface reconstruction: A linear approach," *J. Cogn. Neurosci.*, vol. 5, no. 2, pp. 162–176, 1993.

[2] G. E. Christensen, R. D. Rabbit, M. I. Miller, S. C. Joshi, U. Grenander, T. Coogan, and D. Van Essen, "Topological properties of smooth anatomic maps," in *Proc. Information Processing Medical Imaging (IPMI'95)*, 1995, pp. 101–112.

[3] C. Davatzikos, "Spatial normalization of 3-D brain images using deformable models," *J. Computer-Assisted Tomogr*, vol. 20, no. 4, pp. 656–665, 1996.

[4] P. M. Thompson and A. W. Toga, "A surface-based technique for warping three-dimensional images of the brain," *IEEE Trans. Med. Imag.*, vol. 15, pp. 402–417, Sept. 1996.

[5] ——, "Brain warping," in *Anatomically-Driven Strategies for High-Dimensional Brain Image Warping and Pathology Detection*, A. W. Toga, Ed. New York: Academic, 1998.

[6] S. Sandor and R. Leahy, "Toward automated labelling of the cerebral cortex using a deformable atlas," in *Proc. Information Processing Medical Imaging (IPMI'95)*, 1995, pp. 127–138.

[7] P. M. Thompson, D. MacDonald, M. S. Mega, C. J. Holmes, A. C. Evans, and A. W. Toga, "Detection and mapping of abnormal brain structure with a probabilistic atlas of cortical surfaces," *J. Computer-Assisted Tomogr.*, vol. 21, no. 4, pp. 567–581, 1997.

[8] W. E. Lorensen and H. E. Cline, "Marching cubes: A high-resolution 3-D surface construction algorithm," *ACM Comput. Graph.*, vol. 21, no. 4, pp. 163–170, 1987.

[9] J. F. Mangin, V. Frouin, I. Bloch, J. Regis, and J. Lopez-Krahe, "From 3-D magnetic resonance images to structural representations of the cortex topography using topology preserving deformations," *J. Math. Imag. Vis.*, vol. 5, no. 5, pp. 297–318, 1995.

[10] P. C. Teo, G. Sapiro, and B. A. Wendell, "Creating connected representations of cortical gray matter for functional MRI visualization," *IEEE Trans. Med. Imag.*, vol. 16, pp. 852–863, Dec. 1997.

[11] D. L. Collins, C. J. Holmes, T. M. Peters, and A. C. Evans, "Automatic 3-D model-based neuroanatomical segmentation," *Human Brain Mapping*, vol. 3, pp. 190–208, 1995.

[12] G. E. Christensen, S. C. Joshi, and M. I. Miller, "Volumetric transformation of brain anatomy," *IEEE Trans. Med. Imag.*, vol. 16, pp. 864–877, Dec. 1997.

[13] H. A. Drury, D. C. Van Essen, C. H. Anderson, C. W. Lee, T. A. Coogan, and J. W. Lewis, "Computerized mappings of the cerebral cortex: A multiresolution flattening method and a surface-based coordinate system," *J. Cogn. Neurosci.*, vol. 8, no. 1, pp. 1–28, 1996.

[14] G. J. Klein, P. T. Schoenemann, X. Teng, and T. F. Budinger, "A sensitivity analysis of brain morphometry based on MRI-derived surface models," in *Proc. SPIE Medical Imaging 1998: Physiology Function Multidimensional Images*, 1998, vol. 3337, p. 31.

[15] D. MacDonald, D. Avis, and A. C. Evans, "Multiple surface identification and matching in magnetic resonance images," in *Proc. SPIE Visualization in Biomedical Computing (VBC'94)*, 1994, vol. 2359, pp. 160–169.

[16] C. Davatzikos and R. N. Bryan, "Using a deformable surface model to obtain a shape representation of the cortex," *IEEE Trans. Med. Imag.*, vol. 15, pp. 785–795, Dec. 1996.

[17] S. Sandor and R. Leahy, "Surface-based labeling of cortical anatomy using a deformable atlas," *IEEE Trans. Med. Imaging*, vol. 16, pp. 41–54, Jan. 1997.

[18] C. Xu and J. L. Prince, "Snakes, shapes, and gradient vector flow," *IEEE Trans. Imag. Processing*, vol. 7, pp. 359–369, Mar. 1998.

[19] D. C. Van Essen and J. H. R. Maunsell, "Two-dimensional maps of the cerebral cortex," *J. Comput. Neurology*, vol. 191, pp. 255–281, 1980.

[20] C. Xu, D. L. Pham, and J. L. Prince, "Finding the brain cortex using fuzzy segmentation, isosurfaces, and deformable surface models," in *Proc. Information Processing Medical Imaging (IPMI'97)*, 1997, pp. 399–404.

[21] C. Xu, D. L. Pham, J. L. Prince, M. E. Etemad, and D. N. Yu, "Reconstruction of the central layer of the human cerebral cortex from MR images," in *Proc. Int. Conf. Medical Image Computing and Computer Assisted Interventions (MICCAI'98)*, 1998, pp. 481–488.

[22] A. F. Goldszal, C. Davatzikos, D. L. Pham, M. Yan, R. N. Bryan, and S. M. Resnick, "An image processing protocol for the analysis of MR images from an elderly population," *J. Computer-Assisted Tomogr.*, vol. 22, no. 5, pp. 827–837, 1998.

[23] T. Kapur, W. E. L. Grimson, W. M. Wells III, and R. Kikinis, "Segmentation of brain tissue from magnetic resonance images," *Med. Imag. Anal.*, vol. 1, no. 2, pp. 109–127, 1996.

[24] F. Kruggel and G. Lohman, "Automatical adaption of the stereotactical coordinate system in brain MRI datasets," in *Proc. Information Processing Medical Imaging (IPMI'97)*, 1997, pp. 471–476.

[25] E. L. Chaney and S. M. Pizer, "Defining anatomical structures from medical images," *Seminar Radiation Oncology*, vol. 2, no. 4, pp. 215–225, 1992.

[26] B. R. Condon, J. Patterson *et al.*, "Image nonuniformity in magnetic resonance imaging: Its magnitude and methods for its correction," *Br. J. Radiol.*, vol. 60, pp. 83–87, 1989.

[27] B. M. Dawant, A. P. Zijidenbos, and R. A. Margolin, "Correction of intensity variations in MR images for computer-aided tissue classification," *IEEE Trans. Med. Imag.*, vol. 12, pp. 770–781, Dec. 1993.

[28] D. L. Pham and J. L. Prince, "An adaptive fuzzy c-means algorithm for image segmentation in the presence of intensity inhomogeneities," in *Proc. SPIE Medical Imaging 1998: Image Processing*, 1998, vol. 3338, pp. 555–563.

[29] W. M. Wells III, W. E. I. Grimson, R. Kikinis, and F. A. Jolesz, "Adaptive segmentation of MRI data," *IEEE Trans. Med. Imag.*, vol. 15, pp. 429–442, Aug. 1996.

[30] D. L. Pham and J. L. Prince, "Adaptive fuzzy segmentation of magnetic resonance images," *IEEE Trans. Med. Imag.*, to be published.

[31] ———, "An adaptive fuzzy c-means algorithm for image segmentation in the presence of image inhomogeneities," *Pattern Recognit. Lett.*, vol. 20, no. 1, pp. 57–68, 1999.

[32] C. Montani, R. Scateni, and R. Scopigno, "Discretized marching cubes," in *Proc IEEE. Visualization'94*, 1994, pp. 281–287.

[33] A. D. Kalvin, C. B. Cutting, B. Haddad, and M. Noz, "Constructing topologically connected surfaces for the comprehensive analysis of 3-D medical structures," in *Proc. SPIE Medical Imaging 1991: Image Processing*, 1991, vol. 1445, pp. 247–258.

[34] A. Van Gelder and J. Wilhems, "Topological considerations in isosurface generation," *ACM Trans. Graph.*, vol. 13, no. 4, pp. 337–375, 1994.

[35] M. K. Agoston, *Algebraic Toplogy—A First Course*. New York: Marcel Dekker, 1976.

[36] T. McInerney and D. Terzopoulos, "Deformable models in medical image analysis: A survey," *Med. Imag. Anal.*, vol. 1, no. 2, pp. 91–108, 1996.

[37] M. Kass, A. Witkin, and D. Terzpoulos, "Snakes: Active contour models," *Int. J. Comput. Vis.*, vol. 1, no. 4, pp. 321–331, 1987.

[38] I. Cohen, L. D. Cohen, and N. Ayache, "Using deformable surfaces to segment 3-D images and infer differential structures," *CVGIP: Imag. Under.*, vol. 56, no. 2, pp. 242–263, 1992.

[39] L. D. Cohen and I. Cohen, "Finite-element methods for active contour models and balloons for 2-D and 3-D images," *IEEE Trans. Pattern Anal. Machine Intell.*, vol. 15, pp. 1131–1147, Nov. 1993.

[40] C. Xu and J. L. Prince, "Gradient vector flow: A new external force for snakes," in *Proc. IEEE Conf. Computer Vision Pattern Recognition (CVPR)*, 1997, pp. 66–71.

[41] ———, "Generalized gradient vector flow external forces for active contours," *Signal Processing—Int. J.*, vol. 71, no. 2, pp. 132–139, 1998.

[42] C. Xu, "Deformable models with application to human cerebral cortex reconstruction from magnetic resource images," Ph.D. dissertation, Dept. Electrical Computer Eng., the Johns Hopkins Univ., Baltimore, MD, 1999.

[43] L. D. Cohen, "On active contour models and balloons," *CVGIP: Imag. Under.*, vol. 53, no. 2, pp. 211–218, 1991.

[44] H. Delingette, "Simplex meshes: A general representation for 3-D shape reconstruction," I.N.R.I.A., Sophia-Antipolis, France, Tech. Rep. 2214, 1994.

[45] N. W. Shock, R. C. Greulich, R. Andres, D. Arenberg, P. T. Costa Jr., E. Lakatta, and J. D. Tobin, *Normal Human Aging: The Baltimore Longitudinal Study of Aging*. Washington, D.C.: U.S. Printing Office,1984.

[46] C. A. Cocosco, V. Kollokian, R. K. S. Kwan, and A. C. Evans, "BrainWeb: Online interface to a 3-D MRI simulated brain database," *Neuroimage*, vol. 5, no. 4, 1997.

[47] C. Xu, M. Etemad, D. Yu, D. L. Pham, and J. L. Prince, "A spherical map for cortical geometry," in *Proc. Int. Conf. Functional Mapping Human Brain*, 1998, vol. 7, no. 4, p. 734, 1998.

[48] H. A. Drury and D. C. Van Essen, "Functional specialization in human cerebral cortex analyzed using the visible man surface-based atlas," *Human Brain Mapping*, vol. 5, pp. 233–237, 1997.

[49] D. MacDonald, D. Avis, and A. C. Evans, "Proximity constraints in deformable models for cortical surface identification," in *Proc. Int. Conf. Medical Image Computing Computer Assisted Interventions (MICCAI'98)*, 1998, pp. 650–659.

[50] X. Zeng, L. H. Staib, R. T. Schultz, and J. S. Duncan, "Segmentation and measurement of the cortex from 3-D MR images," in *Proc. Int. Conf. Medical Image Computing Computer Assisted Interventions (MICCAI'98)*, 1998, pp. 519–530.